Thermal Pulse Energy Harvesting

Ian S. McKay and Evelyn N. Wang
Massachusetts Institute of Technology, 77 Massachusetts Avenue, Cambridge, MA 02139, USA

Correspondence: Ian McKay
c/o Theresa Werth 3-461
77 Massachusetts Avenue
Cambridge, MA 02139, USA

ism@mit.edu
1.206.817.2783

Abstract

This paper presents a new method to enhance thermal energy harvesting with pulsed heat transfer. By creating a phase shift between the hot and cold sides of an energy harvester, periodically pulsed heat flow can allow an available temperature gradient to be concentrated over a heat engine during each thermal pulse, rather than divided between the heat engine and a heat sink. This effect allows the energy harvester to work at maximum power and efficiency despite an otherwise unfavorable heat engine-heat sink thermal resistance ratio. In this paper, the analysis of a generalized energy harvester model and experiments with a mechanical thermal switch demonstrate how the pulse mode can improve the efficiency of a system with equal engine and heat sink thermal resistances by over 80%, although at reduced total power. At a 1:2 engine-sink resistance ratio, the improvement can simultaneously exceed 60% in power and 15% in efficiency. The thermal pulse strategy promises to enhance the efficiency and power density of a variety of systems that convert thermal energy, from waste heat harvesters to the radioisotope power systems on many spacecraft.

Keywords: Energy harvesting, thermal energy conversion, thermal pulse, radioisotope power system.

Nomenclature

A Cross-sectional area (m^2)
Bi Biot Number
c Specific heat capacity (J/kgK)
C^* Energy storage ratio $m_S c_S / m_R c_R$
D Duty cycle $t_c/(t_o+t_c)$
Fo Lumped Fourier number $t/(Rmc)$
K Integration constant (K)
L Characteristic length (m)
m Mass (kg)
P Output power (W)
P^* Scaled output power $PR/(T_\infty)$
Q, q Input power (W)
Q^* Scaled power $QR/(T_\infty)$
R Effective thermal resistance (K/W)
R^* Thermal resistance ratio R_s/R_R
T Temperature (K)
T^* Scaled temperature $(T-T_{S,min})/(T_{S,max}-T_{S,min})$
t time (s)
t^* Scaled time t/t_c
α Fraction of Carnot efficiency
∂ Duty ratio t_o/t_c
OTS Oscillating Thermal Switch
PHF Pulsed Heat Flux
RPS Radioisotope Power System

Subscripts:
c Switch closed phase (heat flux on)
E Heat engine
Max Maximum value
Min Minimum value
o Switch open phase (heat flux off)
R Heat rejection
S Heat source
SS Steady-state heat transfer
SW Switch
∞ Ambient condition

1. Introduction

Thermal energy is ubiquitous in nature, and thermal energy harvesters have emerged as a popular choice for many remote power applications [1, 2]. The performance of these systems, however, is often limited by the division of an overall steady-state temperature gradient between a heat engine and a heat sink, which confines the maximum figure of merit to scale with the engine-sink thermal resistance ratio [3, 4]. Since heat sink resistance is typically size-dependent, this limitation is often reflected as a tradeoff between efficiency and power density in energy harvester design [5]. This tradeoff in turn impacts the performance of a variety of crucial thermal systems, including waste heat energy harvesters, combustion-based harvesters used in remote areas, concentrated solar power (CSP) generators, and the radioisotope power systems (RPS) on many spacecraft [1, 5, 6, 7].

The challenge of high rejection-side temperature can be reduced in certain cases if the harvester receives thermal energy in distinct pulses, rather than operating at steady state. By taking advantage of the thermal impedances of the heat source and sink, pulsed heat transfer allows the maximum thermal gradients and heat fluxes in the system to be synchronized. The resulting phase lag between the system hot and cold side temperatures can allow a heat engine to work over a large thermal gradient, despite a conventionally unfavorable engine-sink thermal resistance ratio. This approach theoretically reduces the power and efficiency loss associated with the temperature drop across the heat sink in steady state operation. The thermal pulse mode may therefore enable the development of more effective energy harvesting systems and allow more flexibility in system design, especially for small-scale systems and those that process time-variant heat fluxes. Figure 1 illustrates the effect of the thermal pulse mode schematically, and introduces two methods for inducing pulsed heat transfer.

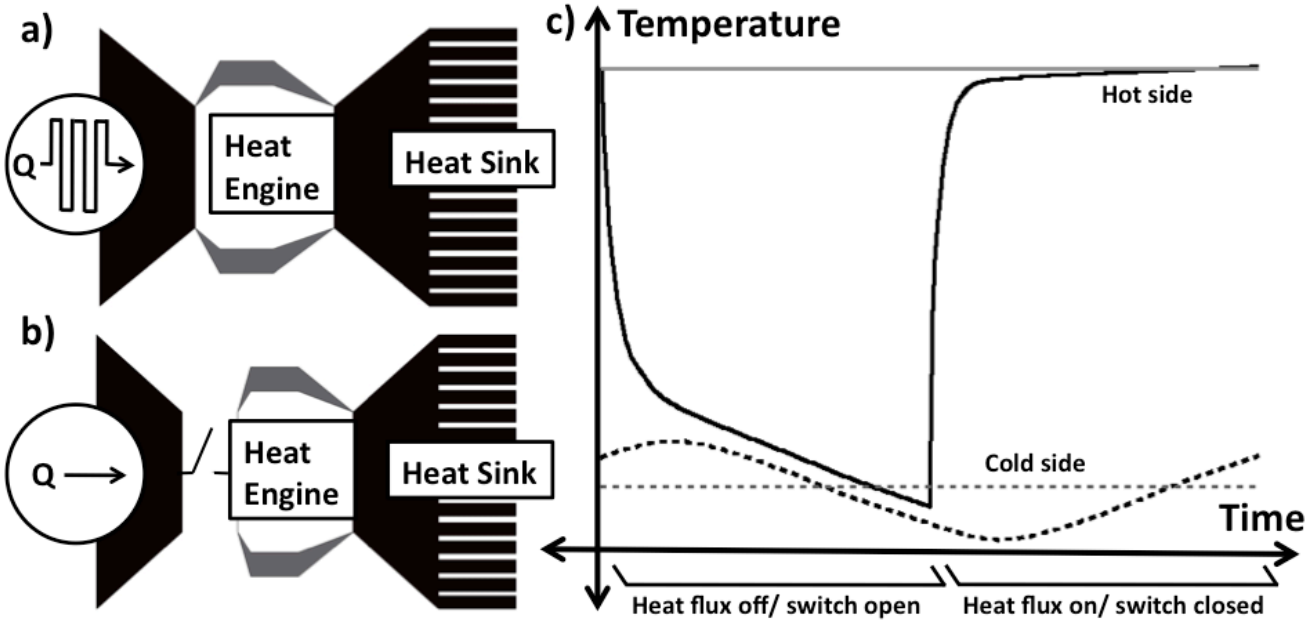

*Figure 1. (left) Generalized energy harvesters using **a)** a pulsed heat source and **b)** an oscillating thermal switch to achieve pulsed heat transfer across a heat engine. **c)** Schematic temperature traces showing heat engine hot side (solid) and cold side (dotted) temperatures with a pulsed heat source (black) and a steady one (gray) with the same time-averaged heat flux Q.*

An energy harvester can operate in a thermal pulse regime either by coupling to a pulsed heat flux (PHF), or by interfacing a constant heat source with an oscillating thermal switch (OTS). Examples of the PHF configuration of Figure 1a include a periodically burning gas heater, intermittently flowing heat transfer fluid, or any other oscillating heat flux. Examples of the OTS configuration shown in Figure 1b include any oscillating thermal connection between a constant heat source and a heat engine, *i.e.*, bistable thermal-fluid circuits such as the Tamburini T-system [8]. The coupling between the hot-side temperature and overall heat flux in the OTS configuration leads to behavior that is distinct from that of the PHF. By cycling between low and high thermal resistance states, the switch acts as variable thermal impedance that in theory generates no entropy. By varying the duty cycle of the switch, the thermal gradient can be adjusted to optimize the conversion efficiency of the heat engine, regardless of the engine thermal resistance or the source heat production.

Thermal transient processes already drive a number of high-efficiency heat removal systems, including pulsating heat pipes [9], solid-state heat pumps [10], and phase change electronics cooling [11]. However, outside of work on pyroelectric and other solid-state phenomena [12, 13], little attention has been given to the potential benefit of the

thermal pulse mode in an energy harvesting context. In this paper, we investigated both the PHF and OTS energy harvesting configurations. We developed a quasi-steady-state model of the pulsed heat flux system in Section 2. A similar model of the OTS (Figure 1b) is developed in Section 3 and validated with proof-of-concept experiments in Section 4. The work shows potential opportunities in using thermal pulse energy conversion for increased efficiency and power output in applications ranging from remote power generation to waste heat recovery.

2. A Pulsed Heat Flux

We developed a generalized lumped model for the PHF configuration (Figure 2a), consisting of a heat source, heat engine, and heat sink. We assume that there is negligible thermal energy storage inside the heat engine, that the internal impedances of the heat source and sink are small relative to that of the heat engine ($Bi << 1$), and that the heat production Q is a continuous square wave, with $Q=Q_o$ for time $0<t<t_c$ and $Q = 0$ from $t_c<t<t_o$, where t_c is the duration of the thermal pulse and t_o the time between pulses. The temperature, mass, and specific heat of the heat source and sink are T_S and T_R, m_S and m_R, c_S and c_R, respectively. The thermal resistances of the heat engine and between the heat sink and ambient are R_E and R_R. Seven non-dimensional parameters describe the PHF system: the engine-sink thermal resistance ratio $R^* = R_E/R_R$, the source-sink energy storage ratio $C^* = m_S c_S / m_R c_R$, power production $Q^* = Q R_E/T_\infty$ and the bulk Fourier numbers $Fo_1 = t_c/(R_E m_S c_S)$ and $Fo_2 = t_o/(R_R m_R c_R)$, which are characteristic heating or cooling time scales for the source and heat sink, respectively. The heat engine efficiency η_E is also defined and assumed to scale by a constant factor α with the Carnot efficiency, $\eta_E = \alpha\,(1-T_R/T_S)$.

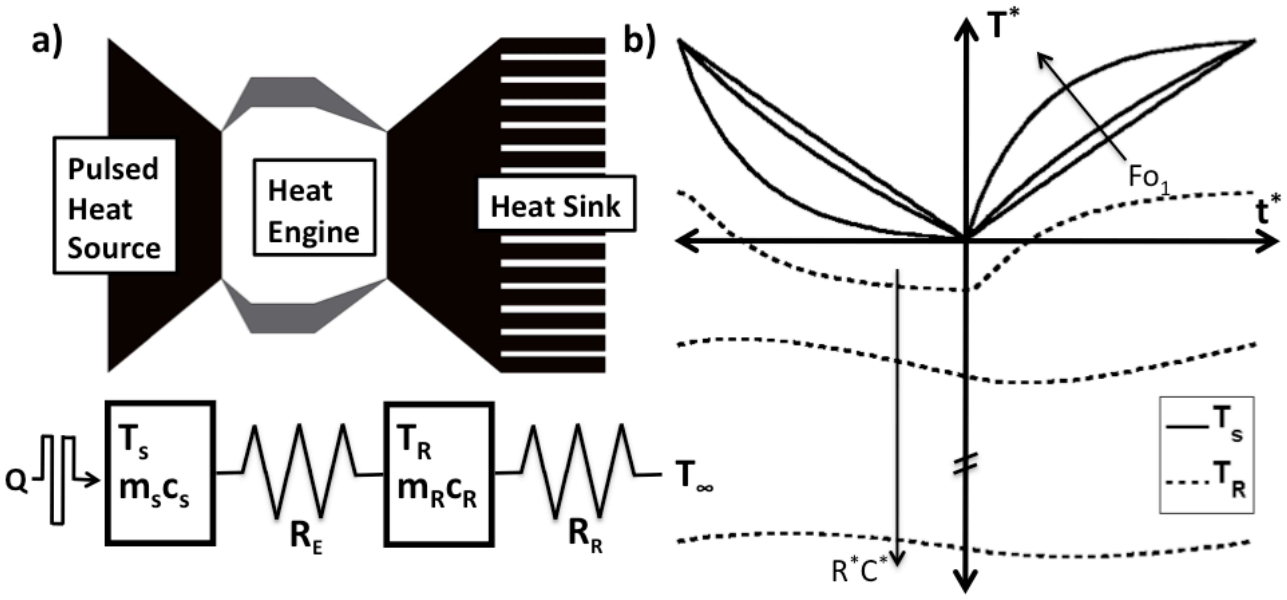

Figure 2. ***a)*** *PHF system (top) and a corresponding lumped-parameter model (bottom).* ***b)*** *Non-dimensional temperature traces of the source and sink, where temperature $T^* = (T-T_{S,min})/(T_{S,max}- T_{S,min})$ and time $t^* = t/t_c$, for temperature swing $(T_{S,max}- T_{S,min})$ and switch closed (heat flux on) time t_c. The traces are shown for different values of the dimensionless time scale Fo_1 and impedance ratio R^*C^*.*

The energy equations that describe the closed (heat flux on) and open (heat flux off) phases are:

$$\left.\frac{dT_S}{dt}\right|_{closed} = \frac{Q}{m_S c_S} - \frac{(T_S - T_R)}{R_E m_S c_S} \tag{1}$$

$$\left.\frac{dT_S}{dt}\right|_{open} = \frac{(T_S - T_R)}{R_E m_S c_S} \tag{2}$$

$$\left.\frac{dT_R}{dt}\right|_{open/closed} = (1-\eta_E)\frac{(T_S - T_R)}{R_E m_R c_R} - \frac{(T_R - T_\infty)}{R_R m_R c_R} \tag{3}$$

The equations are solved recursively, with the initial condition for the closed phase equal to the final condition for the open phase and vice versa. Figure 3a shows the theoretical efficiency of a PHF system normalized to that of a steady-state harvester operating with the same $T_{max}/T_\infty = 1.5$ and $R^*=0.1$, for a variety of the characteristic time scales Fo_1 and Fo_2. Here $R^*=C^*=0.1$ and $\alpha=1$. Figure 3b shows the theoretical output power P of the PHF model for the

same conditions. In each of these simulations, the heat flux Q was set so that the maximum temperature $T_{max} = 1.5\ T_\infty$, so that the analysis applied to real systems with finite maximum hot-side temperatures.

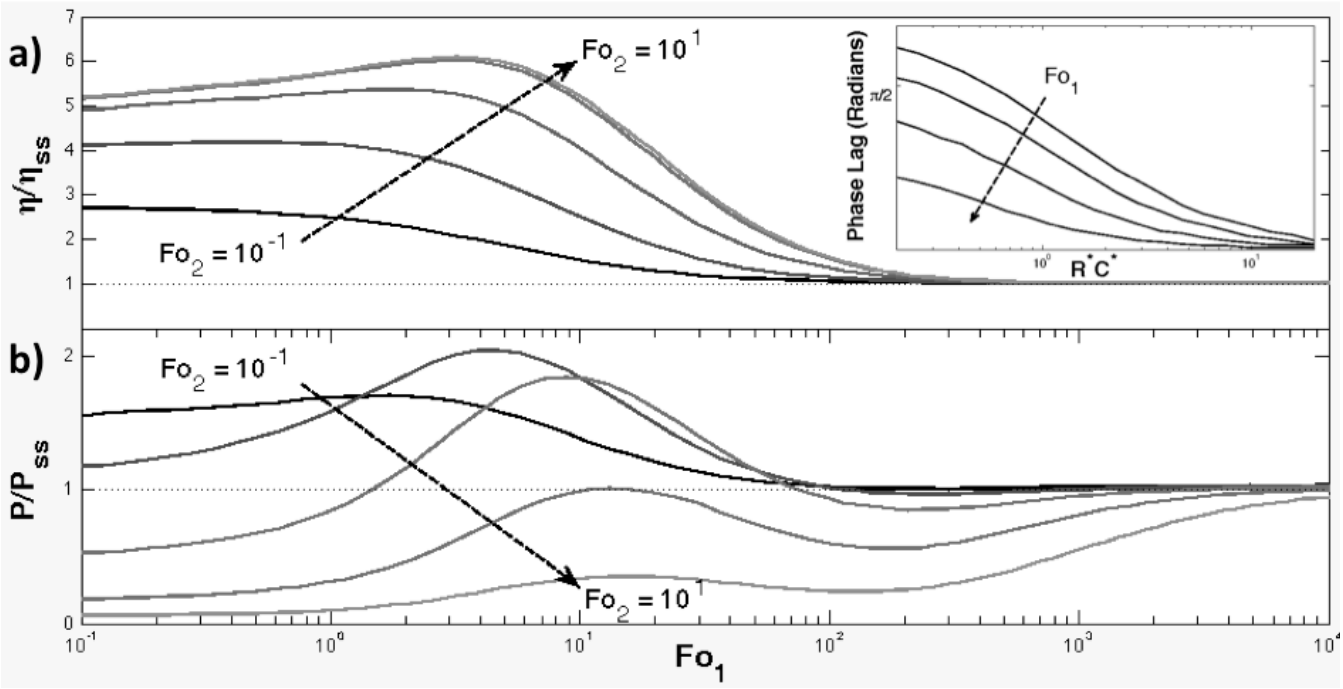

Figure 3. ***a)*** *Efficiency* η *and* ***b)*** *output power P of PHF energy conversion with* Fo_1 *and* Fo_2*, normalized to the steady-state performance* P_{SS} *and* η_{SS} *under the same conditions.* Fo_1 *and* Fo_2 *represent characteristic heat transfer time scales for the heat source and sink, respectively, and vary based on the period and duty cycle of the thermal switch. The traces are given for* $R^*=C^*=0.1$*,* $\alpha = 1$*, and* Q^* *which maintains a hot-side maximum temperature* $T_{max}/T_\infty = 1.5$*. The inset shows the phase lag between the minimum values of the heat source and sink.*

The model indicates that increasing Fo_2 always improves energy conversion efficiency by ensuring that the heat sink has cooled towards T_∞ at the start of each energy conversion cycle. For improved output power, however, the trend is reversed, and shorter Fo_2 is preferred. Both power and efficiency increase with increasing Fo_1 until $Fo_1 \approx 1$, at which point both decay to the steady state value. The inset of Figure 3a shows that the phase lag, defined as the delay in radians between the minimum values of T_s and T_R, are maximized at low Fo_1. However, in this region both power and efficiency are low as a result of lower time-averaged T_s. The optimum for both power and efficiency is at an intermediate Fo_1, where T_s is close to T_{max} for most of the energy conversion phase, and the phase lag is relatively small. The inflection point for both power and efficiency occurs when the product $Fo_1 R^* C^*$, which is associated with the time constant to warm the heat sink, is approximately one.

Figure 4 compares the efficiency and non-dimensional power $P^* = P(R_S+R_R)/T_\infty$ of the PHF and steady-state strategies at the same maximum temperature difference T_{max}/T_∞ for a variety of R^* and C^*. In this figure, $Fo_1 = 5$ and $Fo_2 = 1$, these are near the optimal values for low R^*C^* suggested in Figure 3. Clearly, suitable values of these time scales can allow the PHF exceed the steady state efficiency for almost any system configuration, with over a 50% advantage over steady state η at $R^* = 1$. However, the PHF can only achieve higher power than steady state for systems with low R^*C^*. The power and efficiency boost by $R^* = 0.1$ can exceed 150%, as shown in Figure 3.

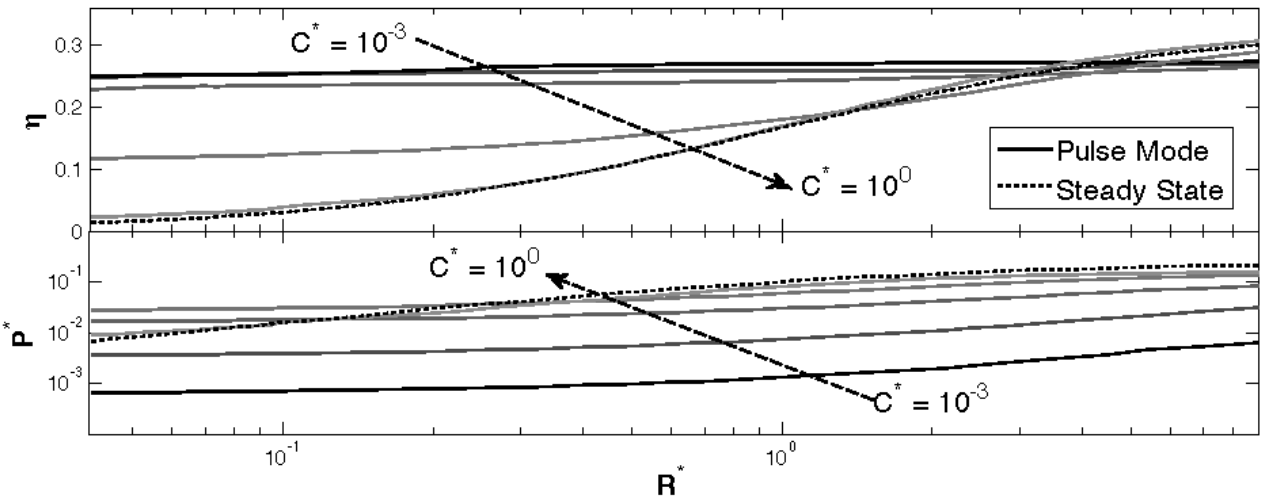

Figure 4. Comparison of the power (bottom) and efficiency (top) of the pulse and steady-state energy conversion regimes for the same hot and cold side temperatures. The traces cover a range of engine-sink resistance ratios R^* and C^*, for intermediate values of the time scales $Fo_1 = 5$, $Fo_2 = 1$.

2.1 Pulsed Temperature Input

An important special case of the PHF model occurs when $Fo_1 << 1$, $C^* << 1$ and the heat flux Q is delivered as sharply declining pulse, as shown in Figure 5. This case corresponds to a square-wave input on the hot side temperature T_S. With T_S specified, the governing equations can be written for T_R alone:

$$\left.\frac{dT_R}{dt}\right|_{closed} = (1 - <\eta_E>)\frac{T_{max} - T_R(t)}{T_E\, m_R\, c_R} - \frac{T_R(t) - T_\infty}{R_R\, m_R\, c_R} \qquad \left(<\eta_E> = \frac{\int_0^{t_c} \alpha(1 - T_R(t)/T_{max})\, dt}{t_c} \right) \tag{4}$$

The boundary conditions are the same as (3). Linearizing the heat engine efficiency $\eta_E = \alpha\,(1 - T_R/T_S)$ over the period t_c yields an analytical expression for T_R:

$$T_R(t) = \frac{R_E T_\infty + R_R T_{max}(1 - <\eta_E>)}{R_E + R_R(1 - <\eta_E>)} + K\, e^{t\,\frac{(R_E + R_R(1 - <\eta_E>))}{m_R\, c_R\, R_R\, R_E}} \qquad \left(K = \frac{-e^{\frac{t_c}{m_R c_R R_R}}\left(e^{\frac{t_o}{m_R c_R R_R}} - 1\right) R_R (T_\infty - T_{max})(1 - <\eta_E>)}{\left(e^{\frac{t_c + t_o}{m_R c_R R_R}} - e^{\frac{t_c(1 - <\eta_E>)}{m_R c_R R_E}}\right)(R_R + R_R(1 - <\eta_E>))} \right) \tag{5}$$

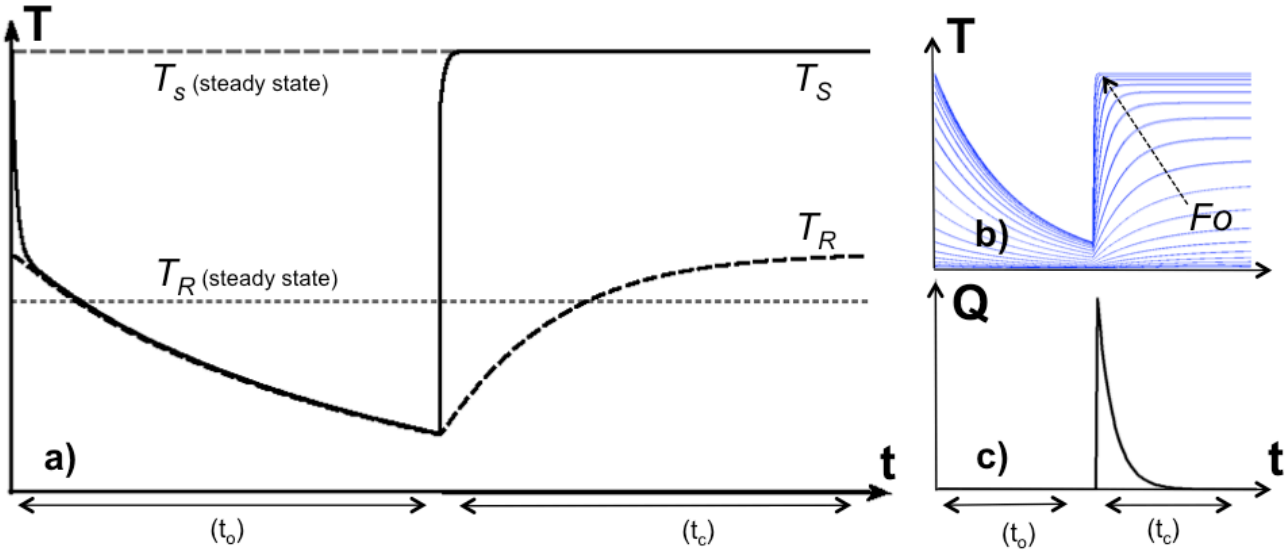

*Figure 5. Schematics of **a)** temperature T_R, **b)** the variation of $T_R(t)$ with Fo, and **c)** thermal input power. All traces are for the special case of small Fo_1 and C^* analyzed in this section. Because this model assumes $T_S = T_R$ during the switch-open phase, it ignores any energy conversion occurring during t_o, and so can only underestimate the ideal power of the thermal pulse mode for small $m_S c_S$ and R_E.*

A characteristic timescale of this system is $Fo = t_c/(R_E m_R c_R)$. As shown in Figure 6, the pulse temperature input results in similar relationships between the timescales δ and Fo and the performance η and P as the pulse heat flux model. However, Figures 6c and 6d clearly show how the square wave temperature input offers better performance than the square wave heat flux input. For optimized δ and Fo, the pulse mode can equal the maximum-power ($R^* = 1$) performance of the steady state mode for any $R^*<1$, and can surpass the steady-state performance in both power and efficiency for all $R^*<1$. This represents an enhancement of approximately 65% in efficiency and 20% in power by $R^* = 0.5$, and nearly a four-fold boost in both power and efficiency by $R^* = 0.1$.

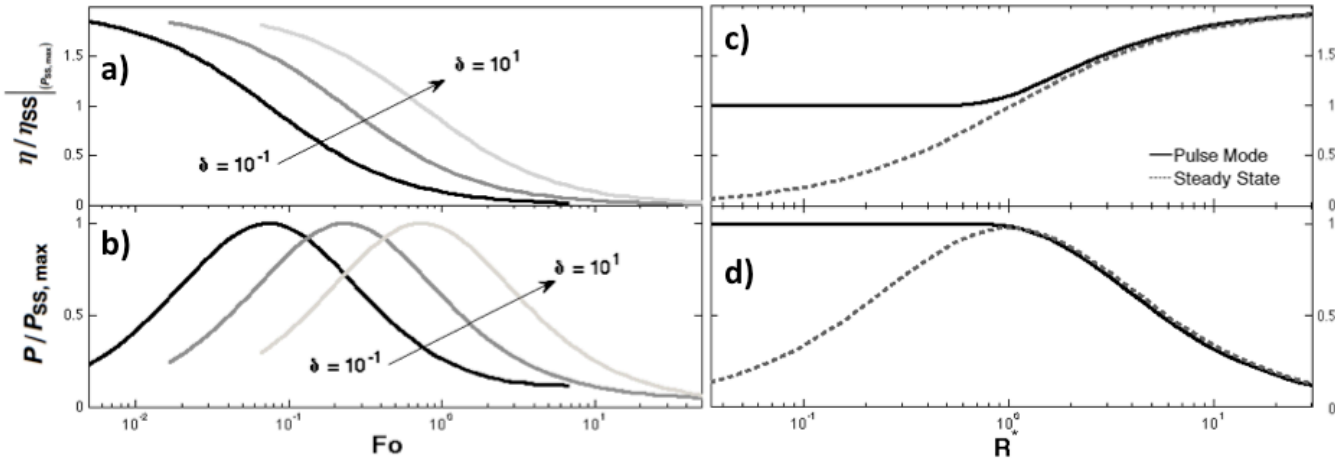

*Figure 6. The variation in **a)** power and **b)** efficiency of the pulsed mode with the actuation timescale Fo, normalized to the maximum power ($R^* = 1$) steady state performance. At suitable Fo, the pulse mode can match or beat the steady state mode in either power or efficiency, but cannot exceed it in both simultaneously. The power and efficiency of both modes are shown relative R^* in **c)** and **d)**, respectively, again relative the steady state performance in the maximum power condition.*

3. An Oscillating Thermal Switch

A second method to achieve pulsed thermal energy conversion is with an oscillating thermal switch positioned between a constant heat source and a heat engine, as shown schematically in Figure 7a. The strategy applies to systems with a contained heat source and thermal energy storage capacity, so that energy is not lost to the surroundings during the switch-open phase. The assumptions underlying the OTS model are the same as for the PHF, with the exception of a constant heat source Q and a lossless and discrete thermal switch between the source and engine.

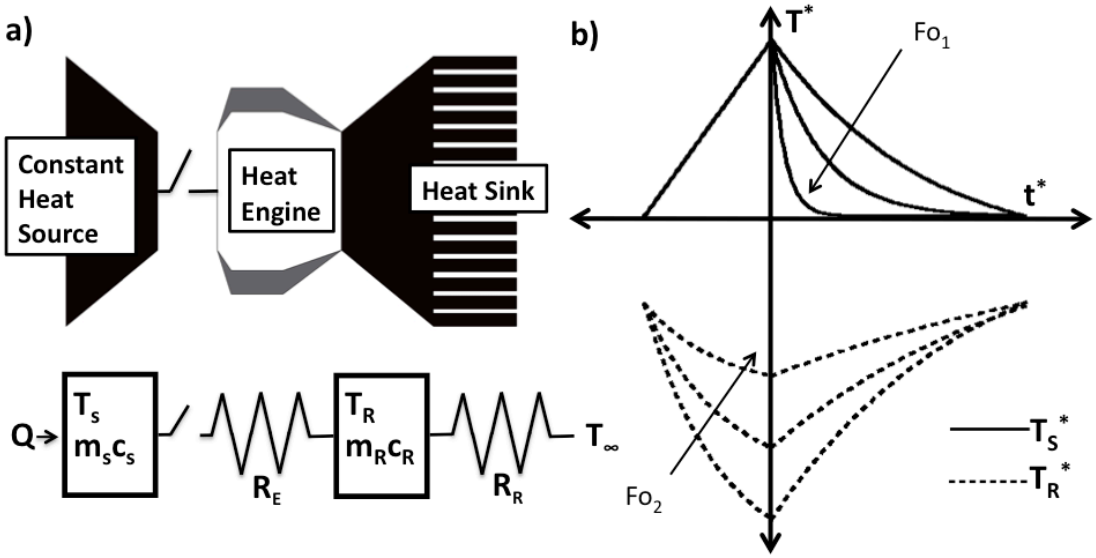

*Figure 7. **a)** OTS system (top) reduced to a lumped-parameter model (bottom). **b)** Non-dimensional temperature traces of the source and sink for different values of the characteristic time scales Fo_1 and Fo_2.*

T_S and T_R for the quasi-steady state OTS system can be described both dimensionally and in terms of the scaled temperature $T^* = (T-T_{S,min})/(T_{S,max}- T_{S,min})$ and time $t^* = t/t_c$:

$$\left.\frac{dT_S}{dt}\right|_{closed} = \frac{Q}{m_S c_S} - \frac{(T_S - T_R)}{R_E m_S c_S} \qquad \left.\frac{dT_S^*}{dt^*}\right|_{closed} = \frac{Fo_1}{Fo_2} R^* C^* - Fo_1(T_S^* - T_R^*) \tag{6}$$

$$\left.\frac{dT_R}{dt}\right|_{closed} = (1-\eta_E)\frac{(T_S - T_R)}{R_E m_R c_R} - \frac{(T_R - T_\infty)}{R_R m_R c_R} \qquad \left.\frac{dT_R^*}{dt^*}\right|_{closed} = Fo_1 C^*[(1-\eta_E)(T_S^* - T_R^*) - R^*(T_R^* - T_\infty^*)] \tag{7}$$

Figure 7b shows schematic traces for T_S^* and T_R^* for different Fo_1 and Fo_2. The first term in (4) is equivalent to the duty ratio $\delta = t_c/t_o$, while in both (4) and (5) the coefficients of the temperature terms are time constants of the switch-closed phase. The boundary conditions are given by the equations for the switch-open phase, when the heat source warms in isolation and the heat sink cools towards T_∞.

$$\left.\frac{dT_S^*}{dt^*}\right|_{open} = \delta \qquad \longrightarrow T_S^*(0) = 1 \tag{8}$$

$$\left.\frac{dT_R^*}{dt^*}\right|_{open} = -Fo_2(T_R^* - T_\infty^*) \qquad \longrightarrow T_R^*(0) = T_\infty^* + (T_R^*(-1/\delta) - T_\infty^*)\, e^{-Fo_2} \tag{9}$$

Figure 8 shows the normalized efficiency and temperature for $C^*=R^*=Q^*=\alpha = 1$. Figure 8a shows that in the absence of a maximum operating temperature, a lower switch duty ratio δ always leads to a higher temperature ratio T_S/T_R, and therefore to more-efficient energy conversion. Figure 8b shows how the minimization of the characteristic time Fo_1 and the maximization of Fo_2 increases the theoretical energy conversion efficiency regardless of the maximum temperature reached.

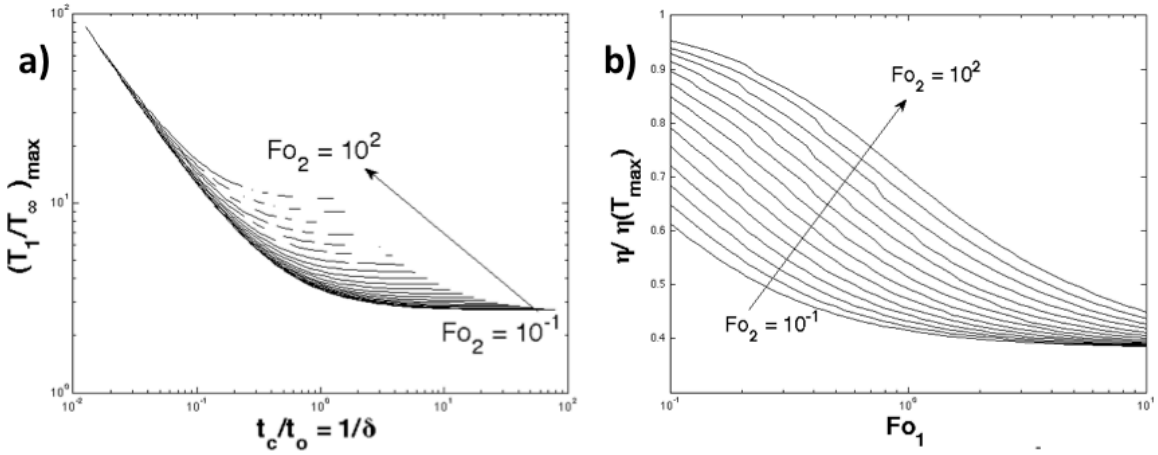

Figure 8. ***a****) Maximum normalized operating temperature as a function of the duty ratio* $\delta = t_o/t_c$ *and* Fo_2. ***b****) Efficiency of the OTS model in terms of the non-dimensional time scales* Fo_1 *and* Fo_2.

The limit of $Fo_1 \ll 1$ and δ, $Fo_2 \gg 1$ corresponds to an operating condition in which the heat sink cools to T_∞ on every switch-open phase and the source temperature remains nearly constant during each switch-closed phase. The maximum efficiency of the OTS model is expected at the maximum possible value of Fo_2 and the minimum value of Fo_1, where δ is set to keep $T_{S,max}$ as close as possible to the temperature tolerance of the system.

3.1 A Special Case: Constant Heat Sink Temperature

Since many energy harvesters are attached to vehicles or other sinks of comparatively large thermal mass, a case where $C^* \approx 0$ and the heat sink temperature is practically constant may be realistic. The $C^* \approx 0$ condition could also reflect the thermal arrest that would result from incorporating a phase change material heat sink. In this case, $T_R = T_\infty + R_R Q$, and the characteristic time scale of the system reduces to Fo_1 alone. This model has a closed-form solution for the energy-conversion temperature gradient T_S/T_R:

$$\frac{T_S}{T_R} = 1 + \frac{Q}{T_R}\left(R_E + \frac{t_o}{m_S c_S}\,\frac{e^{\frac{t_c - t}{R_E m_S c_S}}}{e^{\frac{t_c}{R_E m_S c_S}} - 1}\right) \tag{10}$$

For the maximum efficiency case of $\delta>>1$, $Fo_1<<1$, the temperature simplifies *to* $T_S/T_\infty=1+Q^*(\delta+1)$, and the conversion efficiency is given by $\alpha Q^*/(D+Q^*)$ for duty cycle $D = 1/(\delta+1)$. Because both the source and sink temperatures are effectively constant during the switch-closed phase with $Fo_1<<1$, the temperature gradient reflects the effective thermal resistance of a rapidly switched connection with resistance R_{sw} between two infinite thermal reservoirs: $R_{Eff} = R_{sw}/D$. For a $C^* \approx 0$ system operating in these conditions, the maximum temperature T_{max} corresponds to the duty cycle $D = Q^*/(T_{max}/T_\infty - 1)$.

4. Experimental Validation

We conducted proof-of-concept experiments to both validate the model and investigate the potential of the OTS strategy. In one set of experiments, a $C^* = 0$ test apparatus was used to validate equation (8) and the maximum efficiency case over a range of Fo. In a second set of experiments, we compared an OTS system at favorable Fo_1 and Fo_2 to an equivalent steady-state system for a variety of R^* and C^*, while limiting both systems to the same maximum temperature.

As shown in Figure 9a, an externally-powered latching solenoid (Shenzhen Appliances ZHO-1253) was used to physically move a heated block into and out of contact with either a thermoelectric generator (Marlowe TG-12) connected to a large heat sink for the $C^* = 0$ case shown, or with a simulated heat engine-heat sink combination (for the general case). A compliant graphite-polymer interface (Panasonic PGS) was used to ensure identical contact resistance for both the steady-state and OTS tests. The tests were conducted in a vacuum chamber at a pressure under 500 Pa to minimize convective heat loss. In both cases, the temperatures T_S and T_R were measured using a J-type thermocouple and used to infer the energy conversion potential of the simulated heat engine; the thermoelectric generator was left in an open-circuit condition to ensure constant thermal resistance, preserving the generality of the results.

4.1 Constant Heat Sink Temperature

For the constant heat sink temperature case, the duty cycle of the connection was calibrated to keep the maximum temperature of the heat source constant at $T_{max}/T_\infty = 1.25$ during steady oscillation. This experiment confirmed the interdependence of Fo_1 and η, for the case where $\alpha = 1$, $C^* = 0$ and $Q^* = .01$ from the model. The theoretical maximum efficiency was calculated from the average of η_{Carnot} over the heat flux. Figure 9b shows the experimental results compared with both the exact solution and the approximation $\eta = \alpha Q^*/(D+Q^*)$. As shown, the exact solution is in good agreement with the actual performance. The small discrepancy is likely due to a combination of imperfect thermal isolation of the simulated heat source, parasitic contact resistance on the hot-side compliant thermal interface, finite thermal gradients inside the heat sink, and unaccounted-for effects of the thermal energy storage in the simulated heat engine, which would bring the solution closer to the $D = 1$ behavior. The error bars are associated with the standard deviation in calculated η between successive energy conversion periods, and which can be attributed to the imperfect components used to set t_c and t_o.

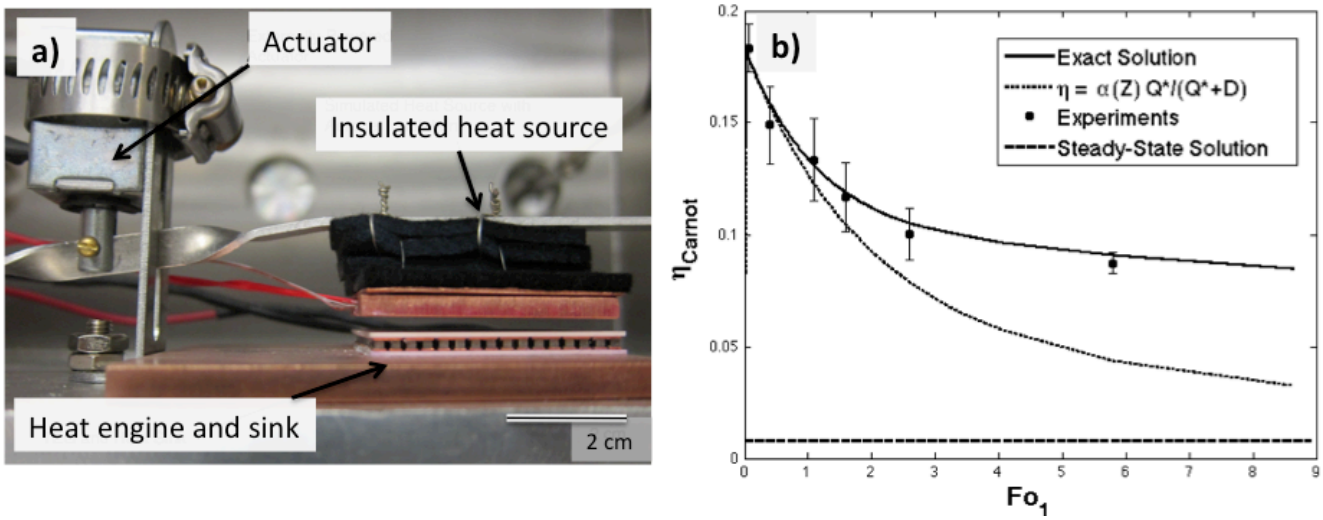

Figure 9 a) *Proof-of-concept experiment in a vacuum chamber.* ***b)*** *Average energy conversion efficiency η_{Carnot} based on experimental temperature measurements for the oscillating switch system ($\alpha = 1$, $C^* = 0$, $Q^* = .01$), showing the convergence to the approximate conversion efficiency $\eta = \alpha Q^*/(D+Q^*)$ when $Fo_1 <<1$. In the thermal pulse tests, D was set to maintain $T_{max}/T_\infty = 1.25$.*

4.2 A General Oscillating Thermal Switch

This test evaluated the OTS strategy for a system with a real heat sink, $C^* \neq 0$, for a variety of R^*. We modified the demonstration of Figure 9a to include two thermal resistors and a copper block in place of the thermoelectric generator, emulating the engine resistance R_E, heat sink resistance R_R, and heat sink thermal mass $m_S c_S$, respectively. The test apparatus was painted black to enable quantitative temperature measurement with an infrared camera (measured temperatures were verified with a J-type thermocouple). The actuation time scales were set to the near-optimal $Fo_1 = 0.1$ and $Fo_2 = 10$, and the heat flux Q set such that the maximum temperature ratio T_{max}/T_∞ did not exceed 1.5 at any point in the actuation cycle. Monitoring both T_S and T_R, we were then able to compare the steady-state and OTS performance for a variety of R^* and C^*. Figure 10 shows an infrared image the modified apparatus, highlighting the higher average energy conversion temperature gradient of the OTS strategy relative to the steady-state strategy. Figure 11 shows the variation in η with R^* in this test, highlighting the ability of the OTS system to maintain near-optimal efficiency for a range of system configurations.

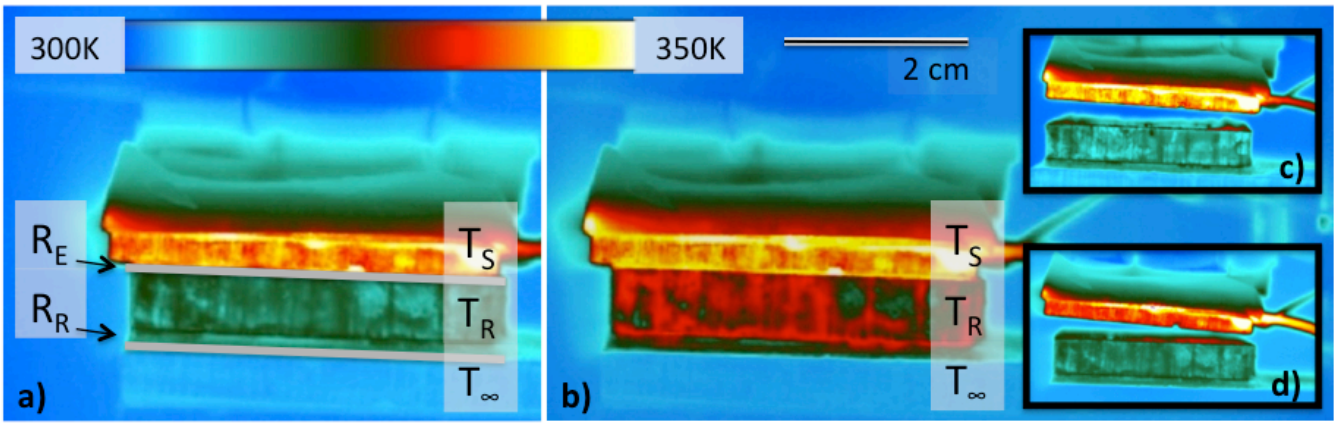

Figure 10. *Infrared image of the modified test system, showing the two inert thermal resistors placed between the source, heat sink, and ambient blocks.* ***a)*** *The thermal gradient during the middle of the switch-closed phase of the OTS cycle thermal gradient for $C^* = 0.5$, $R^* = 1$ and $T_{max}/T_\infty = 1.15$.* ***b)*** *The steady-state temperature profile for the same conditions. The inset shows the OTS system an instant before (**c**) and an instant after (**d**) the switch-closed period.*

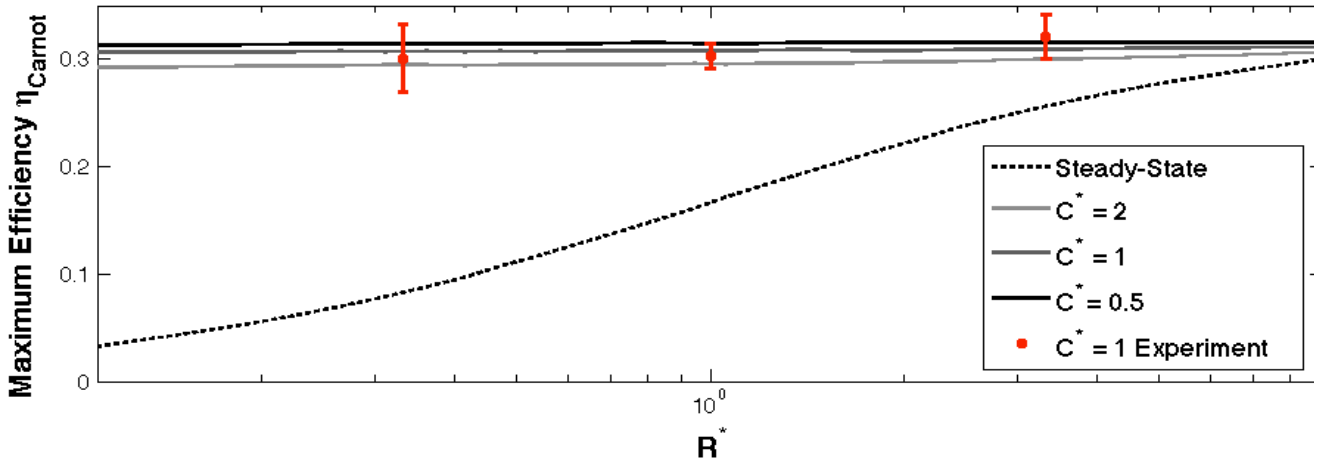

Figure 11. *Performance comparison between the OTS and steady-state energy harvesting strategies for a variety of C^* and R^*, all held to $T_{max}/T_\infty = 1.5$ and working at quasi-optimal $Fo_1 = 0.1$, $Fo_2 = 10$. The experimental results are for a $C^* = 1$ system similar to that in Figure 10.*

Figure 11 confirms that the OTS strategy has considerable efficiency advantages over steady-state heat flow over a range of R^*. However, these advantages should be understood in context of the lower power of the OTS system. Due to the higher effective thermal resistance of the OTS connection, an OTS system with a given maximum hot-side temperature must process a lower time-averaged heat flux than an identical system without a thermal switch. For the PHF model, this effect can be overcome by running the system at lower R^* and delivering heat in short bursts, enabling high power operation. In contrast, the maximum heat flux over the engine in the OTS model is coupled to the heat source temperature T_S. As a result, given a maximum hot-side temperature, the OTS can improve energy conversion efficiency over an optimized steady-state strategy, but at the expense of lower specific power.

5. Discussion

We developed two models of thermal pulse energy conversion, one based on a periodic heat flux (PHF), and another based on a periodic connection to a constant heat source (OTS). Additionally, two important sub-cases were investigated, representing thermal switching to constant hot- and cold-side temperatures, respectively. For a fixed system resistance R_R+R_E and temperature bounds T_{max} and T_∞, the OTS strategy is ideally suited to increase the energy conversion efficiency at low power across a range of R^*, and its high and variable thermal impedance could also help small systems maintain a higher hot-side temperature than is typically possible. In contrast, the PHF strategy is capable of increasing both efficiency and power, though the combination of the two cannot exceed the steady-state maximum. While the behavior of the PHF and OTS systems differ, in both cases the energy conversion enhancement is attributable to effective adjustment in R_E with changing D.

The best performance is expected from a system with a pulsed hot-side temperature input (Section 2.1). For a system limited by heat rejection capacity, this strategy theoretically allows an energy harvester work at the system maximum power point (ordinarily possible only at $R^* = 1$) at any R^*. Just as the OTS, it also enables the system to approach the maximum possible efficiency $\eta_E = \alpha\,(1-T_\infty/T_{max})$ at any R^*, although at a lower power.

These attributes could allow for better performance and design flexibility for systems otherwise compromised by unfavorable R^*. Such systems include very small-scale energy harvesters, in which R_E cannot be elevated enough to compensate for low heat rejection ability. Energy harvesters that process time-variant heat fluxes could also be enhanced; for these systems, an adjustment in D to match the incident flux would constitute a new type of thermal maximum power point tracking.

While the thermal pulse mode may be best-suited to small-scale energy harvesters, the application to more traditional systems is also of interest. Figure 12 shows generalized schematics of two such systems. The gas-fired chiller in Figure 12a represents a direct application of the PHF model of Section 2. Figure 12b depicts a general energy converter, such as a solar-thermal power plant using a PHF strategy. By cycling heat transfer fluid between two engine-heat sink pairs, the system could benefit from the efficiency boost of the PHF without the power loss even at higher R^*. In a variant of Figure 12b, the PHF might also be implemented with a naturally oscillatory conversion process, such as in pyroelectric or thermochemical converters [11, 15]. Promising future work might include an analysis of the thermal pulse mode in the context of one of these oscillatory conversion processes.

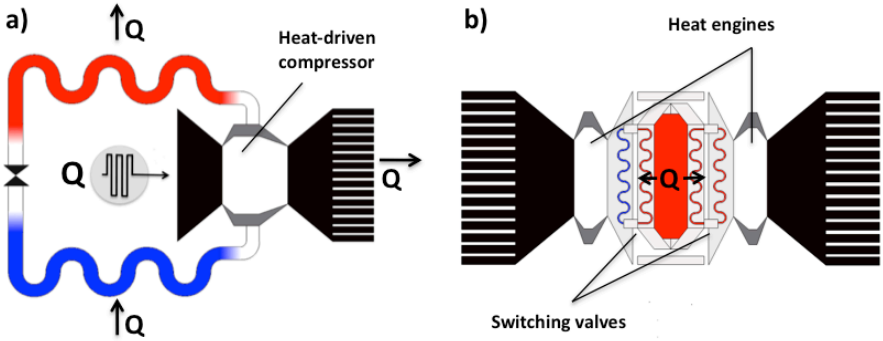

Figure 12. a) *Example application of thermal pulse energy conversion in a gas-fired chiller.* ***b)*** *The thermal pulse strategy in an energy harvester that uses a constant heat source, such as an RPS. This system could run with a single heat engine if the switch were instead used to cycle coolant between two heat sinks. In* ***a)****, the periodic heat transfer is induced by switching the combustor on and off. In* ***b)****, the periodic heat transfer could be induced with a switching valve, or with one of the passively bistable thermal-fluid circuits described in [2].*

6. Conclusions

This paper presents a new method of enhancing thermal energy conversion with pulsed heat transfer. In the transient regime, an available temperature difference can be more effectively concentrated across a heat engine, rather than split between the heat engine and a heat sink. If controlled properly, this effect can be exploited to increase both the efficiency and power density of systems that operate with a low engine-heat sink resistance ratio R^*. The enhancement increases at lower R^*, where traditional conversion strategies break down. The theoretical efficiency improvement for a system with $R^* = 1$ could exceed 80% with reduced output power, while the improvement for an $R^* = 0.5$ system could exceed 60% in power and 15% efficiency, without any increase in the system hot-side temperature. The maximum efficiency of the pulsed heat flux model occurs at the maximum possible value of the time scale Fo_2, low Fo , and the duty cycle D that keeps T_S as near as possible to the maximum temperature. The maximum power is also reached at low Fo_1, but at more intermediate Fo_2 and higher D. The high and variable thermal impedance of the periodic thermal connection may be particularly useful for systems that work at small scales or with time-varying heat production. Future work may include an expanded treatment of the governing equations tailored towards a specific type of thermal energy harvester, or an analysis of suitable methods of inducing pulsed heat transfer from a constant heat source.

References

[1] Gur I, Sawyer K, Prasher R. Searching for a better thermal battery. Science 2012 335(1).
[2] Hall, W. Terrestrial applications of thermoelectric generators. Handbook of thermoelectrics CRC Press 1995; 503-
[3] Sonntag R, Borgnakke C, Wylen G. Fundamentals of thermodynamics 6th ed. John Wiley and Sons 2003; 232
[4] Bierschenk J. Optimized thermoelectrics for energy harvesting applications. Energy harvesting technologies. Springer 2009; 337-349
[5] Snyder G. Thermoelectric energy harvesting. Energy harvesting technologies. Springer 2009; 325-336
[6] Mason L. Realistic specific power expectations for advanced radioisotope power systems. Journal of propulsion and power 2007; 23(5): 1075-1079
[7] Wagner M, Kutscher C. Assessing the impact of heat rejection technology on CSP plant revenue. SolarPACES 2010;
[8] Weislogel M. Passive oscillatory heat transport systems. AIP Conf. Proc. 2002; 608: 241-248
[9] Akachi H. Structure of a heat pipe, US Pat. No. 4,921,041, 1991
[10] Snyder G, Fleurial J, Caillat T, Yang R, Chen G. Supercooling of peltier cooler using a current pulse. Journal of applied physics 2002; 92[3]: 1564-9
[11] Kandasamy R, Wang X, Mujumdar A. Transient cooling of electronics using phase change material (PCM)-based heat sinks. Applied thermal engineering 2008, 28(8-9)
[12] Hunter N, Lavrick N, Bannuru T, Mostafa A, Rajic S, Datskos P. Development of MEMS-based pyroelectric thermal energy harvesters. Proc. of SPIE 2011; 8035: 80350V
[13] Choi W, Hong S, Abrahamson J, Han J, Changsik C, Nair N, Baik S, Strano M. Chemically driven carbon-nanotube-guided thermopower waves. Nature Materials 2010; 9(5): 423–9
[14] Incropera F, Dewitt D, Bergman L, Lavine A. Introduction to heat transfer, 5th ed, John Wiley & Sons, 2007;485
[15] Vining C, Williams R, Underwood M, Ryan M, Suitor J. Reversible thermodynamic cycle for AMTEC power conversion. J. Electrochem. Soc. 1993; 140(10):2760-2763.